

## Article

# Defining the URCOTEBS System as a Unilateral Radiographic–Stochastic Model for the Complementary States (Health/Disease) of the D-Organ and Middle-Ear Mucosa

Marian Rădulescu<sup>1,†</sup>, Adela-Ioana Mocanu<sup>2,\*</sup>, Alexandra-Cristina Neagu<sup>3,†</sup> , Mihai-Adrian Schipor<sup>4</sup>  
and Horia Mocanu<sup>5,\*</sup> 

- <sup>1</sup> Department of ENT&HNS, Faculty of Medicine, “Carol Davila” University of Medicine and Pharmacy, 020021 Bucharest, Romania
- <sup>2</sup> Department of ENT&HNS, Polimed Medical Center, 040067 Bucharest, Romania
- <sup>3</sup> Department of ENT&HNS, “Marie Sklodowska Curie” Emergency Children’s Hospital, 041434 Bucharest, Romania; aaaneagu30@yahoo.com
- <sup>4</sup> Institute of Astronomical and Physical Geodesy, Technical University of Munich, 80333 Munich, Germany; mihai.schipor@unibw.de
- <sup>5</sup> Department of ENT&HNS, Faculty of Medicine, “Titu Maiorescu” University, 031593 Bucharest, Romania
- \* Correspondence: adela.mocanu@polimed.ro (A.-I.M.); horia.mocanu@prof.utm.ro (H.M.); Tel.: +40-723400435 (A.-I.M.); +40-732662268 (H.M.)
- † These authors contributed equally to this work.

**Abstract:** The middle ear (ME) is a notoriously complicated anatomic structure, geometrically arranged as irregular interlinked spheroidal and polyhedral cavities dug inside the temporal bone (TB). The bony walls of these cavities are radiopaque and form the bony support for the *D-Organ* that we have previously defined as corresponding to the epithelium covering the Antrum walls (belonging to the central cavities of the middle ear) and the walls of mastoid and petrous cavities (the peripheral cavities of the ME). The aim of the study is to define an exact method for categorizing a Unilateral Radiographic CONformation of the TEmporal Bone in Schuller’s projection (URCOTEBS) under one of the four defined conformations and using it for practical everyday clinical purposes. The conclusion is that a radiograph in Schuller’s projection is a concrete way of storing precise information on the status (health/disease) of the *D-Organ* and therefore of the ME mucosa. These data is encoded within the image and we aim to decode and translate them into clinical data. The URCOTEBS results in an overlapping projection of all bony cavities that comprise the General Endo-temporal Bony Cavity Complex onto the same plain (film). This characteristic of classical film imaging constitutes an advantage from the multiple CT sections, as far as our proposed approach goes, because the set of stochastic information is found in the whole of the cavities taken as one on the same image, to which the measurement gauges can be easily applied. The decoding must be performed accordingly, and this occurs much faster with conventional radiography. This image of the TB in Schuller’s projection is a mirror that reflects the status of the ME mucosa, and URCOTEBS encodes the physiological state of the *D-Organ*. The present work gives, through stochastic methods, the key to decoding this information into clinical language. In ascending order of their projection areas (projection of their *Variable Geometry Peripheral Endo-temporal Bony Cavity Complex*) we can recognize URCOTEBS\_d, URCOTEBS\_c, URCOTEBS\_b, and URCOTEBS\_a. The corresponding Greek letter designates the state of disease for each of these conformations: URCOTEBS\_δ, URCOTEBS\_γ, URCOTEBS\_β, URCOTEBS\_α, and the capital letters define their state of health: URCOTEBS\_D, URCOTEBS\_C, URCOTEBS\_B, URCOTEBS\_A. URCOTEBS\_d is the smallest unilateral radiographic conformation of the TB in Schuller’s projection and is, by definition, a radiographic image of the state of disease of the D-Organ. The probability of disease in URCOTEBS\_d is 100%. This radiographic system is readily available and clinically usable.

**Keywords:** radiology; X-rays; tomography; otitis media; ventilation; anatomy; physiology; statistical modeling



**Citation:** Rădulescu, M.; Mocanu, A.-I.; Neagu, A.-C.; Schipor, M.-A.; Mocanu, H. Defining the URCOTEBS System as a Unilateral Radiographic–Stochastic Model for the Complementary States (Health/Disease) of the D-Organ and Middle-Ear Mucosa. *Appl. Sci.* **2023**, *13*, 12861. <https://doi.org/10.3390/app132312861>

Academic Editors: Cecilia Surace and Alice Berardo

Received: 23 October 2023  
Revised: 26 November 2023  
Accepted: 28 November 2023  
Published: 30 November 2023



**Copyright:** © 2023 by the authors. Licensee MDPI, Basel, Switzerland. This article is an open access article distributed under the terms and conditions of the Creative Commons Attribution (CC BY) license (<https://creativecommons.org/licenses/by/4.0/>).

## 1. Introduction

The *D-Organ* is a unistratified epithelial cellular population of homogenous morphology supported by a basilar membrane on top of a conjunctive structure that provides vascularization and innervation. The final layer of this conjunctive structure is the periosteum that binds it to the subjacent bone, which we will term the *Variable Geometry Anatomic Macroscopic Radiopaque Peripheral Support of the D-Organ*. This bony structure is geometrically arranged as irregular interlinked spheroidal and polyhedral cavities that form a common enclosure of completely determined volume  $V_\epsilon$  [1,2]. The bony walls of these cavities form the aforementioned bony support. It is self-evident that these walls alone are dense enough to provide a radiographic image (for ease of description and writing we shall term this radiopaque); the cavities they define are radiolucent and contain a mix  $\epsilon$  of  $\sigma$  types of respiratory gases saturated with water vapors representing a thermodynamic system  $\epsilon^T$  completely defined by the three state parameters ( $p_\epsilon, V_\epsilon, T_\epsilon$ ) and delimited from its external environment (interface) by the unistratified epithelium called the *D-Organ* [1,2].

Each of these cavities communicates with at least six others (the six directions of space), which means that each cavity communicates, directly or indirectly, to all others thus forming the *Variable Geometry Peripheral Endo-temporal Bony Cavity Complex*, a term subservient to the larger term *Variable Geometry Peripheral Middle Ear* (Figure 1a,b). This complex communicates to the *Non-variable Geometry Central Axial Bony Cavities of the Middle Ear*, which in turn is subordinated to the notion of *Non-variable Geometry Central Axial Middle Ear*. The communication takes place through the corresponding orifices found in the walls of these central cavities (*Antrum, Additus, Protympanum, Tympanic cavity*)—Figure 2.

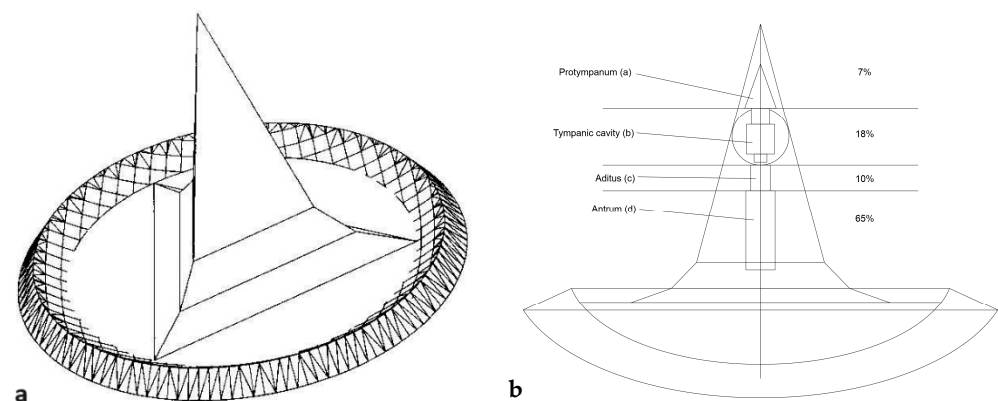


**Figure 1.** (a) Three-dimensional view of the regular composed geometric body representing the geometric-statistic model for the adult temporal bone [2]. (b) Longitudinal axial section through the geometric body representing the geometric-statistic model for the adult temporal bone. We can observe the position and fraction between the non-variable (central) and variable geometry middle ear (peripheral) [2].

The *F-Organ* is made up of a population of *F-Cells* whose *Anatomic Macroscopic Radiopaque Peripheral Support* is represented by the walls of the *Non-variable Geometry Central Axial Bony Cavities of the Middle Ear*, except the Antrum, which supports one of the *two D-Cell subpopulations* [1,2]. Thus, the cardinal of *F-Cell population* remains constant throughout a person's postnatal life and is two orders of magnitude smaller than the cardinal of *D-Cell population*. Practically, we will consider the middle-ear mucosa as a unit and the pathogenic and surface contribution of the *F-Cell population* insignificant by comparison to *D-Cell population* [1,2].

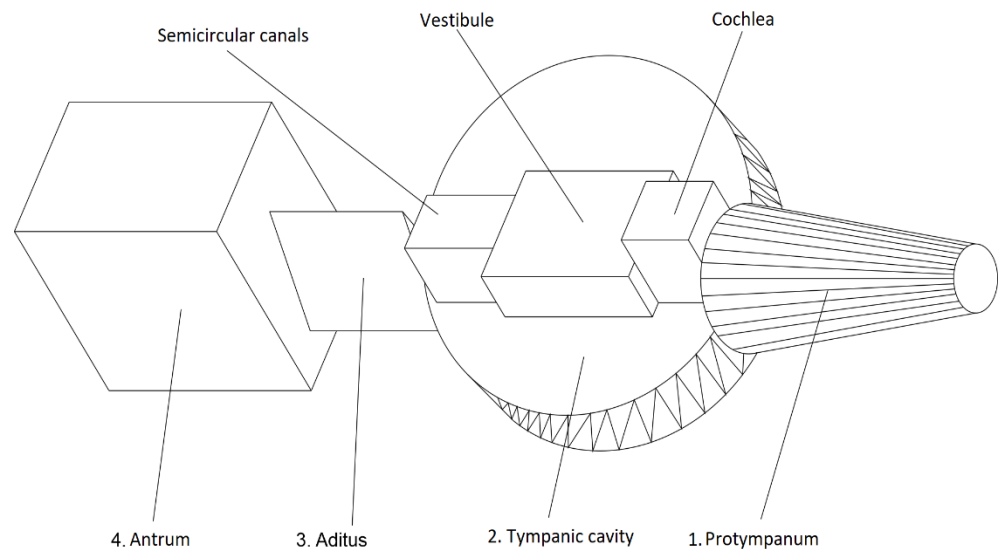


**Figure 2.** Three-dimensional representation of the fixed geometry middle ear and inner ear according to the geometric model of the temporal bone [2].

We can now define the *D-Organ* (general *D-Cell* population) as a sum of two subpopulations of *D-Cells*:

- *Central Axial D-Cell Subpopulation* of constant cardinal that has as *Anatomic Macroscopic Radiopaque Bone Support* the luminal surface of the Antrum—the size of this surface is constant throughout the subject’s life starting from the seventh fetal month, and the cardinal of this subpopulation is constant and much smaller (by two orders of magnitude) than the other conspecific subpopulation.
- *Peripheral D-Cell Subpopulation* of variable cardinal that has as *Anatomic Macroscopic Radiopaque Bone Support* the variable geometry peripheral middle ear. The size of this surface grows or stops growing depending on the ratio of diseased *D-Cells*. The cardinal of this subpopulation is two orders of magnitude larger than the other conspecific subpopulation.

The *D-Cell* is a rectangular prism-shaped epithelial cell of minimal dimension (height  $h^D$ ), perpendicular to the basilar membrane of the epithelium and the maximum dimension ( $l^D$ ) parallel to the basilar membrane [1,2]—Figure 3.

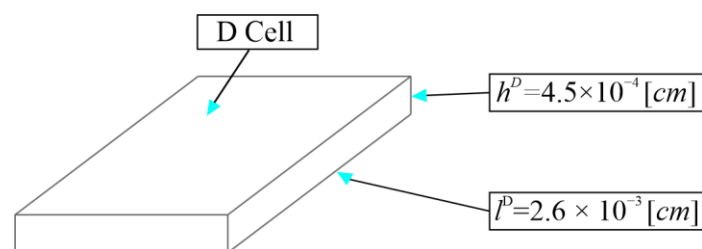


**Figure 3.** Statistic-geometric model for the *D-Cell*.

From a stochastic perspective, the *D-Cell* represents the statistical unit of the *D-Cell* general population (the cardinal of *D-Cells* comprising the *D-Organ*).

From a physiological point of view, each *D-Cell* is a functional unit of the *D-Organ* and it works as an energy consuming ionic membrane pump, working against trans-membrane and trans-cellular pressure gradients to transfer the three respiratory gas species (molecular oxygen, carbon dioxide, molecular nitrogen) from the internal environment of the human body into the middle-ear cavities. More precisely, there are three species of trans-membrane pumps corresponding to the three species of respiratory gases, all exclusively localized

within the luminal membrane of the cell (one of the six surfaces of the cellular membrane) that faces the peripheral cavities of the middle ear (including the Antrum). This membrane is permeable to passive diffusion of respiratory gases (the  $F^*$ -Function of the  $D$ -Cell) [1,2] according to Fick's law, similar to all membranes of the other human cells. The  $F$ -Organ fulfills the  $F$ -Function, which means the passive diffusion of respiratory gas molecules from the cavities of the ME into the internal environment of the body according to pressure gradients governed by Fick's law [1,2].

From a geometric, stochastic, and radiologic perspective, the  $D$ -Organ represents the sum of all  $D$ -Cells or the static general population of  $D$ -Cells. Axiomatically, we consider that the  $D$ -Cell can only be in one of the two complementary states: functional (Healthy) or non-functional (Diseased). We have previously stated that a halt in mastoid growth (*Variable Geometry Peripheral Endo-temporal Bony Cavity Complex*—Figure 2) occurs when the number of diseased  $D$ -Cells ( $D$ -function abolished) lays within the closed interval  $[0.28; 0.5]$ . The mastoid keeps growing as long as the number of diseased  $D$ -Cells is within the closed interval  $[0; 0.27]$ . The unilateral radiographic examination of the temporal bone (mastoid) in Schuller's projection shows the degree of development (growth) of the *Variable Geometry Peripheral Endo-temporal Bony Cavity Complex*, which is the *Variable Geometry Anatomic Macroscopic Radiopaque Peripheral Support of the D-Organ* and therefore the *Variable Geometry Anatomic Macroscopic Radiopaque Peripheral Support of the Middle-ear Mucosa*.

We would like to point out that this is osseous support and is defined by variable geometric sizes. These sizes are in themselves precise information on the status (health/disease) of the  $D$ -Organ and therefore of the ME mucosa. Thus, this bony structure is the material support for information encoded in its geometrical sizes and the radiographic image of the structure is the transcription of this stochastic information on film. The conclusion is that a radiograph in Schuller's projection is a concrete way of storing information on the status (health/disease) of the  $D$ -Organ and therefore of the ME mucosa. These data is encoded within the image and we aim to decode and translate them into clinical data.

The unilateral radiographic examination of the temporal bone (mastoid) in Schuller's projection results in an overlapping projection of all bony cavities that comprise the *General Endo-temporal Bony Cavity Complex* onto the same plain (film), and this constitutes an advantage from the multiple CT sections because the set of stochastic information is found in the whole of the cavities taken as one. The decoding must be performed accordingly, and this occurs much faster with conventional radiography, although other imagistic methods such as CT-scan and sometimes MRI are considered the standard in today's medicine.

## 2. Materials and Methods

In our previous article, we postulated that the state of the  $D$ -Organ (health/disease) can be statistically quantitatively defined, which gives the possibility of explaining the disease of the  $D$ -Organ (*Chronic Inflammation of the ME Mucosa*) through probability theory and mathematical statistics (stochastic).

We define chronic inflammation as a pathological status determined by irreversible intracellular lesions that annihilate the  $D$ -Function [1,2]. This is equivalent to total and permanent functional incapacity of the  $D$ -Cell exclusively in regard to the  $D$ -Function. All other cellular functions, including the  $F^*$ -Function, remain normal. This means that

$$\begin{aligned} \text{Diseased D-Cell} &\equiv \text{Non-functional D-Cell (permanent loss of D-Function)} \equiv \\ \text{D-Cell with irreversible lesions} &\equiv \text{D-Cell with chronic lesions.} \end{aligned} \quad (1)$$

$$\text{Healthy D-Cell} \equiv \text{Functional D-Cell.}$$

As a consequence, the *Chronic Inflammatory Disease of the ME Mucosa* is equivalent to the disease status of the  $D$ -Organ, a status previously defined by quantitative statistical methods (1). We can state  $D$ -Organ disease when the specific weight of non-functional  $D$ -Cells is equal or higher than 28% but lower or equal to 50%. The principle behind this has been enunciated over 200 years ago by the French physician and surgeon *François Joseph*



Victor Broussais (1772–1838), who advocated the identity between physiology and pathology and that diseases are merely the effects of simple changes in intensity in the action of the stimulants that are indispensable for maintaining health [3,4]. This idea will be later on adopted by the philosopher and sociologist *Isidore Marie Auguste François Xavier Comte* (1798–1857), who postulated that the identity of the normal and the pathological is affirmed as the acquisition of knowledge about the normal [4,5], and by the father of experimental physiology and founder of experimental medicine, *Claude Bernard* (1813–1878), who, on the contrary, moves from the normal to the pathological with the aim of rational action directed at the pathological [4–6]. Broussais stated that all disease is an inflammation and irritation of tissues, especially of the digestive tract. He also invents the principle of identity between normal and pathologic, the only difference being of a quantitative nature. Acute inflammation is a totally reversible status that also may interest the *D-Organ* at times but only transitory and without permanent effects. There is no filiation between the two types of inflammations (reversible/irreversible–acute/chronic) and therefore there is no pathogenic linkage between the acute disease of the ME (acute otitis media) and chronic disease of the ME (chronic otitis media), which we especially term *Chronic Inflammatory Disease of the ME Mucosa* to make this distinction.

The fact that the status of the *D-Organ* is completely defined by two closed numerical intervals  $\{[0; 0.27]; [0.28; 0.5]\}$  representing the weight of *D-Cells* with irreversible lesions demonstrates that we are dealing with random mass phenomena that can be studied through probability theory and statistics. The essential characteristic of these phenomena is stability (consistency) of occurrence frequency.

The nature of the pathological agents and their interaction with the *D-Cells* interests us only to the extent where we can define the sum “*S*” of all conditions that ensure that the discussed events are *random, independent, and mass* events. The outside agent capable of producing a chronic lesion has, in itself, nothing special apart from the chance of interacting at a given time with the *D-Cells* (statistic units of a given population). By outside agent, we mean outside of the *D-Cell*, both surrounding environment and inside the subject’s body. We will disregard the biological nature of the studied events (assailant agents, interaction between agents and cells, results of such interactions) and we will only calculate the odds (probability) of such events occurring (odds of assailant agents coming in contact with cells and odds of producing chronic irreversible lesions).

*Question 1—What is the probability that an assailant agent comes into contact with the cells of the D-Organ?* This is a complete set of events formed by two complementary (incompatible, opposing) events:  $E_1 = \text{YES}$  [comes into contact];  $E_2 = \text{NO}$  [does not come into contact], which leads to the equality of the two probabilities  $P(E_1) = P(E_2) = 1/2$ . The two events form the certain event partitioning, which means the concomitant existence of the assailant agent and *D-Organ*.

*Question 2—What is the probability that once in contact to the D-Cell the assailant agent interacts or does not interact with it?* This is also a complete set of events similar to the previous, formed by two complementary (incompatible, opposing) events:  $E_3 = \text{YES}$  [it interacts];  $E_4 = \text{NO}$  [does not interact], which leads to the equality of the two probabilities  $P(E_3) = P(E_4) = 1/2$ . This is the certain event partitioning, which means the potential existence of interaction between the assailant agent and *D-Cells* (implicitly *D-Function*).

*Question 3—starting from the two previous answers, we propose the following problem:*

Using the *unreplaced ball principle*, also known as *hypergeometric distribution* [7,8] (Figure 4), let us calculate the probability of obtaining random events with the following experiment: in an urn there are 50 black balls and 100 white balls (the ratio signifies the biological defense mechanisms of the *D-Cell* against any type of aggression—if the assailant agent interacts with the cell, the chances of irreversible damage are 50%); we extract 100 balls from the urn without returning any of them (*the unreturned ball*). Determine the probability of achieving a series of 25 independent, random events, meaning the pairs of integer numbers starting with 2 black balls–98 white balls and continuing with 4 black balls–96 white balls, 6 black balls–94 white balls . . . all the way to 50 black balls–50 white balls.

**The unreplaced ball principle:** if inside an urn there are balls of  $m$  colors:  $a_1$  of color  $c_1$ ;  $a_2$  of color  $c_2$ ;  $a_m$  of color  $c_m$ , and if we extract  $n$  balls concomitantly (or one by one without returning the extracted ball inside the urn), then the probability of obtaining  $\alpha_1$  balls of color  $c_1$ ,  $\alpha_2$  balls of color  $c_2$ ,  $\alpha_m$  balls of color  $c_m$  ( $\alpha_1 + \alpha_2 + \dots + \alpha_m = n$ ) is:

$$\frac{C_{a_1}^{\alpha_1} C_{a_2}^{\alpha_2} \dots \cdot C_{a_m}^{\alpha_m}}{C_{a_1+a_2+\dots+a_m}^{\alpha_1+\alpha_2+\dots+\alpha_m}}$$

**Figure 4.** The unreturned ball principle.

The number of black balls represents the weight of chronically diseased *D-Cells* (irreversible). This status is determined by the interaction between the assailant agent and the *D-cell* population and is assessed as such at the end of all contact between the two entities. The number of white balls represents the weight of healthy *D-Cells* (complementary), also assessed at the end of all contact between the two entities.

We have axiomatically conferred to the body’s defense mechanism and therefore to the *D-Cell* also the intrinsic capacity to cut the chances of assailant success (irreversible lesions) in half: 100 white balls versus 50 black balls. This means that *Question 3* can be stated as follows: Determine the probability of achieving a series of 25 independent, random events completely defined by 25 pairs of integer numbers representing the weight of complementary diseased and healthy *D-Cells* ( $\text{Weight}_{\text{diseased cells}} = 1 - \text{Weight}_{\text{healthy cells}}$ ). These 25 events represent the partition of the event  $E_1 = \text{YES}$  [comes into contact] with an already known probability of  $1/2$  and 25 possible manners of intensity of said aggression. These probabilities are valid for a single *D-Cell* population forming a single *D-Organ* located in the temporal bone of a single individual. To obtain information regarding the general human population or a segment thereof, the corresponding temporal bone population (one-side), and the corresponding *D-Organ* population for these TBs, we must calculate the probabilities of achieving each of these 25 events this time considered as Exclusive Random Events. We shall use Poisson’s scheme [9,10] (Figure 5). In other words, we must calculate the probability of having one of the 25 Independent Random Events without having any of the other (see Table 1).

**Poisson’s scheme**

If independent events  $A_1, A_2, \dots, A_n$  have known probabilities:  $P(A_1) = p_1; P(A_2) = p_2; P(A_n) = p_n$ ; then the probability of having  $k$  events out of the  $n$  (and not have  $n-k$ ) is the coefficient  $x^k$  from the polinomyal  $Q(x)=(p_1x + q_1)(p_2x+q_2)\dots(p_nx+q_n)$ ; where  $q_i=1-p_i; i=1, 2, \dots, n$ . The probability of this event occuring is:

$$\sum p_{i_1} \cdot p_{i_2} \dots \cdot p_{i_k} q_{i_{k+1}} \dots \cdot q_{i_n}$$

**Figure 5.** Poisson’s scheme.

**Table 1.** Probabilities of achieving the 25 Random Exclusive Events calculated with the unreturned ball scheme and Poisson’s scheme.

Event Index	White Balls (Weight of Healthy D-Cells)	Black Balls (Weight of Diseased D-Cells)	Event	Primitive Probability (Unreturned Ball Scheme and Poisson’s Scheme)	Corrected Primitive Probability (Brought to 1/2 )
1	2	3	4	5	6
1	98	2	98_2	$2.46 \times 10^{-10}$	$1.23 \times 10^{-10}$
2	96	4	96_4	$5.67 \times 10^{-9}$	$2.84 \times 10^{-9}$
3	94	6	94_6	$8.22 \times 10^{-8}$	$4.11 \times 10^{-8}$
4	92	8	92_8	$8.41 \times 10^{-7}$	$4.20 \times 10^{-7}$
5	90	10	90_10	$6.47 \times 10^{-6}$	$3.23 \times 10^{-6}$
6	88	12	88_12	$3.90 \times 10^{-5}$	$1.95 \times 10^{-5}$
7	86	14	86_14	$1.89 \times 10^{-4}$	$9.46 \times 10^{-5}$
8	84	16	84_16	$7.54 \times 10^{-4}$	$3.77 \times 10^{-4}$
9	82	18	82_18	$2.50 \times 10^{-3}$	$1.25 \times 10^{-3}$
10	80	20	80_20	$7.02 \times 10^{-3}$	$3.51 \times 10^{-3}$
11	78	22	78_22	$1.67 \times 10^{-2}$	$8.36 \times 10^{-3}$
12	76	24	76_24	$3.42 \times 10^{-2}$	$1.71 \times 10^{-2}$
13	74	26	74_26	$6.03 \times 10^{-2}$	$3.01 \times 10^{-2}$
14	72	28	72_28	$9.21 \times 10^{-2}$	$4.61 \times 10^{-2}$
15	70	30	70_30	$1.22 \times 10^{-1}$	$6.12 \times 10^{-2}$
16	68	32	68_32	$1.42 \times 10^{-1}$	$7.10 \times 10^{-2}$
17	66	34	66_34	$1.44 \times 10^{-1}$	$7.21 \times 10^{-2}$
18	64	36	64_36	$1.28 \times 10^{-1}$	$6.41 \times 10^{-2}$
19	62	38	62_38	$1.00 \times 10^{-1}$	$5.01 \times 10^{-2}$
20	60	40	60_40	$6.88 \times 10^{-2}$	$3.44 \times 10^{-2}$
21	58	42	58_42	$4.15 \times 10^{-2}$	$2.08 \times 10^{-2}$
22	56	44	56_44	$2.20 \times 10^{-2}$	$1.10 \times 10^{-2}$
23	54	46	54_46	$1.03 \times 10^{-2}$	$5.15 \times 10^{-3}$
24	52	48	52_48	$4.22 \times 10^{-3}$	$2.11 \times 10^{-3}$
25	50	50	50_50	$1.52 \times 10^{-3}$	$7.62 \times 10^{-4}$
Sum of calculated probabilities				100%	50%

The complementary event to  $E_1$  is  $E_2 = \text{NO}$  [does not come into contact], also with a 1/2 probability. This one is equivalent to the 100% weight of healthy *D-Cells* and also 0% weight of diseased *D-Cells*. To facilitate this, the last event we discuss had the index 0 and was called Event 100\_0 (100% white balls, 0% black balls)—see Table 2. This finally defines a complete system of 26 Exclusive Random Events of known probabilities (Table 2).

**Table 2.** Probabilities of the complete 26 Exclusive Random Events system.

Event Index	White Balls (Weight of Healthy D-Cells)	Black Balls (Weight of Diseased D-Cells)	Event	Primitive Probability (Unreturned Ball Scheme and Poisson’s Scheme)	Corrected Primitive Probability (Brought to 100%)
1	2	3	4	5	6
0	100	0	100_0	$5.00 \times 10^{-1}$	$5.00 \times 10^{-1}$
1	98	2	98_2	$2.46 \times 10^{-10}$	$1.23 \times 10^{-10}$
2	96	4	96_4	$5.68 \times 10^{-9}$	$2.84 \times 10^{-9}$
3	94	6	94_6	$8.24 \times 10^{-8}$	$4.12 \times 10^{-8}$
4	92	8	92_8	$8.43 \times 10^{-7}$	$4.21 \times 10^{-7}$
5	90	10	90_10	$6.48 \times 10^{-6}$	$3.24 \times 10^{-6}$

Table 2. Cont.

Event Index	White Balls (Weight of Healthy D-Cells)	Black Balls (Weight of Diseased D-Cells)	Event	Primitive Probability (Unreturned Ball Scheme and Poisson's Scheme)	Corrected Primitive Probability (Brought to 100%)
6	88	12	88_12	$3.91 \times 10^{-5}$	$1.95 \times 10^{-5}$
7	86	14	86_14	$1.89 \times 10^{-4}$	$9.47 \times 10^{-5}$
8	84	16	84_16	$7.55 \times 10^{-4}$	$3.78 \times 10^{-4}$
9	82	18	82_18	$2.50 \times 10^{-3}$	$1.25 \times 10^{-3}$
10	80	20	80_20	$7.03 \times 10^{-3}$	$3.52 \times 10^{-3}$
11	78	22	78_22	$1.67 \times 10^{-2}$	$8.37 \times 10^{-3}$
12	76	24	76_24	$3.43 \times 10^{-2}$	$1.71 \times 10^{-2}$
13	74	26	74_26	$6.04 \times 10^{-2}$	$3.02 \times 10^{-2}$
14	72	28	72_28	$9.23 \times 10^{-2}$	$4.61 \times 10^{-2}$
15	70	30	70_30	$1.22 \times 10^{-1}$	$6.11 \times 10^{-2}$
16	68	32	68_32	$1.42 \times 10^{-1}$	$7.11 \times 10^{-2}$
17	66	34	66_34	$1.44 \times 10^{-1}$	$7.21 \times 10^{-2}$
18	64	36	64_36	$1.28 \times 10^{-1}$	$6.41 \times 10^{-2}$
19	62	38	62_38	$1.00 \times 10^{-1}$	$5.01 \times 10^{-2}$
20	60	40	60_40	$6.89 \times 10^{-2}$	$3.45 \times 10^{-2}$
21	58	42	58_42	$4.16 \times 10^{-2}$	$2.08 \times 10^{-2}$
22	56	44	56_44	$2.20 \times 10^{-2}$	$1.10 \times 10^{-2}$
23	54	46	54_46	$1.03 \times 10^{-2}$	$5.16 \times 10^{-3}$
24	52	48	52_48	$4.23 \times 10^{-3}$	$2.11 \times 10^{-3}$
25	50	50	50_50	$1.52 \times 10^{-3}$	$7.61 \times 10^{-4}$
Sum of calculated probabilities				1.50	1.00

We notice that the first 14 events in Table 2 (0, 1, 2, . . . , 13) correspond to the definition of Healthy *D-Organ* and the last 12 to the Diseased *D-Organ* [1,2]. Event number 14 represents the minimum weight of diseased cells, starting from which the growth of the *D-Organ* comes to a halt [2]. This event is the key to explaining the entire phenomena. The status of the *D-Organ* corresponding to event 14 (Exclusive Event 72\_28) will be completely determined if it can be identified with its physical (geometric) and functional (metabolic energy consumption of a *D-Cell*,  $q_i$ ) status at the time of birth (the *D-Organ* becomes functional starting from the seventh fetal month) [1].

During intra-uterine life, any of the abovementioned events is axiomatically considered as *impossible events* (probability 0). If we admit this postulate, then the moment of birth is defined as a benchmark (numerical value 1) for the functional status (metabolic energy consumption necessary for *D-Function*) and anatomic (number of *D-Cells*) status, reflected by the geometric measures of the *Endo-temporal Bony Cavity Complex* and the *Anatomic Macroscopic Radiopaque Bony Support of the D-Organ*. In other words, we confer the numerical value 1 to the two characteristics of the *D-Organ* considered at the moment of birth: metabolic energy consumption and geometric measurements.

Starting from this and based on *Geometric–statistical model for middle-ear anatomy and ventilation* [2] (Figure 6) and the *Thermodynamic Model for Middle-Ear Ventilation* [1], we can determine a matrix based on the data from the 26 Exclusive Random Events with their corresponding probabilities (Table 3). The connection between this data matrix and practice (clinical) is the unilateral radiograph of the TB under Schuller’s projection (the geometrical measurements belonging to the said matrix)—see Table 3, column 8.

The starting point for this connection is the axiomatic definition of the equivalency between the series of the last 12 events (E14–E25) in the data matrix to any experimental series of the smallest unilateral radiographic images of the *Endo-temporal Bony Cavity Complex* and the *Anatomic Macroscopic Radiopaque Bony Support of the D-Organ* or of the smallest unilateral radiographic conformations of the TB in Schuller’s projection (URCOTEBS), which we will note as **URCOTEBS\_d**. This series of events completely defines the state of disease.

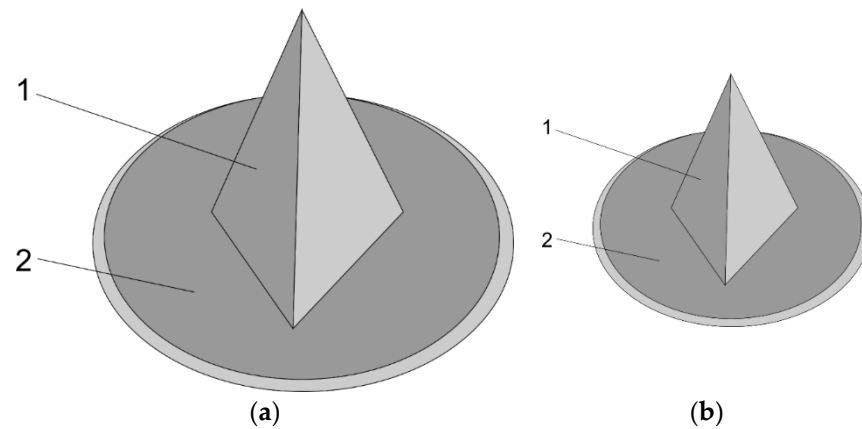


**Figure 6.** (a) Three-dimensional representation of the temporal bone according to the geometric model for an adult: 1—right pyramid with a triangular base; 2—spherical cap. (b) Three-dimensional representation of the temporal bone according to the geometric model for a newborn: 1—right pyramid with a triangular base; 2—spherical cap.

**Table 3.** Data matrix.

Event Index	Event	Unilateral Radiographic Conformation of the Temporal Bone in Schuller’s Projection	White Balls (Weight of Healthy D-Cells) [%]	Black Balls (Weight of Diseased D-Cells) [%]	Corrected Primitive Probability (from the Unreturned Ball Scheme and Poisson’s Scheme) (Brought to 100%)	Energy Consumption Relative to Consumption at the Time of Birth	Total Volume of Pneumatized Cavities Relative to the Volume at the Time of Birth
1	2	3	4	5	6'	7	8
0	100_0	a	100	0	$5.00 \times 10^{-1}$	3%	6.00
1	98_2	a	98	2	$1.23 \times 10^{-10}$	6%	5.64
2	96_4	a	96	4	$2.84 \times 10^{-9}$	9%	5.29
3	94_6	a	94	6	$4.12 \times 10^{-8}$	12%	4.93
4	92_8	a	92	8	$4.21 \times 10^{-7}$	15%	4.57
5	90_10	a	90	10	$3.24 \times 10^{-6}$	18%	4.21
6	88_12	b	88	12	$1.95 \times 10^{-5}$	21%	3.86
7	86_14	b	86	14	$9.47 \times 10^{-5}$	24%	3.50
8	84_16	b	84	16	$3.78 \times 10^{-4}$	28%	3.14
9	82_18	b	82	18	$1.25 \times 10^{-3}$	31%	2.79
10	80_20	b	80	20	$3.52 \times 10^{-3}$	34%	2.43
11	78_22	c	78	22	$8.37 \times 10^{-3}$	37%	2.07
12	76_24	c	76	24	$1.71 \times 10^{-2}$	40%	1.71
13	74_26	c	74	26	$3.02 \times 10^{-2}$	43%	1.36
14	72_28	d	72	28	$4.61 \times 10^{-2}$	100.00%	1
15	70_30	d	70	30	$6.11 \times 10^{-2}$	103%	1
16	68_32	d	68	32	$7.11 \times 10^{-2}$	106%	1
17	66_34	d	66	34	$7.21 \times 10^{-2}$	109%	1
18	64_36	d	64	36	$6.41 \times 10^{-2}$	112%	1
19	62_38	d	62	38	$5.01 \times 10^{-2}$	115%	1
20	60_40	d	60	40	$3.45 \times 10^{-2}$	118%	1
21	58_42	d	58	42	$2.08 \times 10^{-2}$	121%	1
22	56_44	d	56	44	$1.10 \times 10^{-2}$	124%	1
23	54_46	d	54	46	$5.16 \times 10^{-3}$	128%	1
24	52_48	d	52	48	$2.11 \times 10^{-3}$	131%	1
25	50_50	d	50	50	$7.61 \times 10^{-4}$	134%	1
Sum of calculated probabilities					1.00		

The matrix also completely defines the other three types of unilateral radiographic conformations of the TB in Schuller’s projection (URCOTEBS), which we termed in ascending order of their projection areas (projection of their *Variable Geometry Peripheral Endo-temporal Bony Cavity Complex*): **URCOTEBS\_c**, **URCOTEBS\_b**, **URCOTEBS\_a**. This definition is,



after all, the concatenation of the matrix data based on the scaling theory and classification theory. Also note that we used the corresponding Greek letter to designate the state of disease for each of these conformations: **URCOTEBS<sub>δ</sub>**, **URCOTEBS<sub>γ</sub>**, **URCOTEBS<sub>β</sub>**, **URCOTEBS<sub>α</sub>**, and capital letters for their state of health: **URCOTEBS<sub>D</sub>**, **URCOTEBS<sub>C</sub>**, **URCOTEBS<sub>B</sub>**, **URCOTEBS<sub>A</sub>**.

Table 4 presents the complete definitions of the four radiographic conformations, each representing an Exclusive Random Event and having its own probability. The stability (consistency) of this probability is the essential characteristic of Random Mass Events. By mass, we understand both the *D-Cell population* and also any general human population. Thus, Random Mass Events have a defining general tendency toward constancy of probability achievement.

**Table 4.** Data matrix concentrated on defining the unilateral radiographic conformations of the TB in Schuller’s projection through mean numerical values of the energy and volume contribution, as well as the weight of healthy and diseased D-Cells.

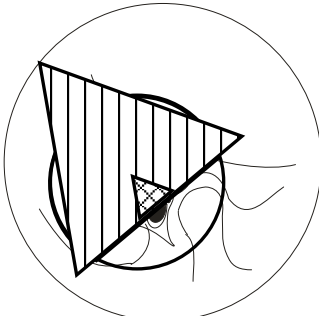
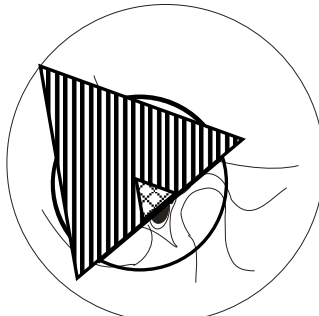
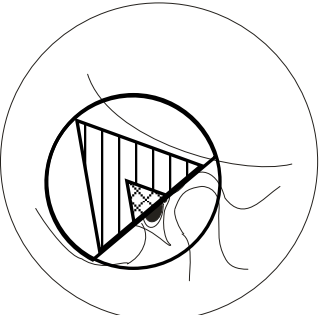
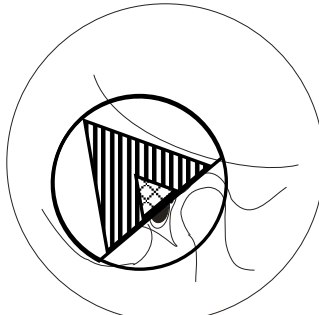
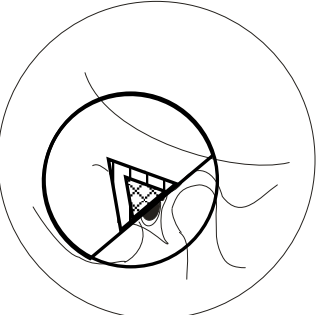
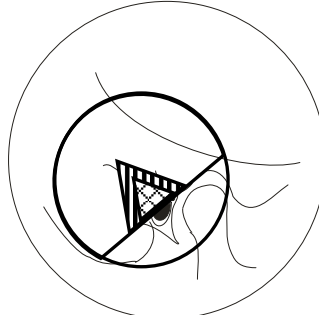
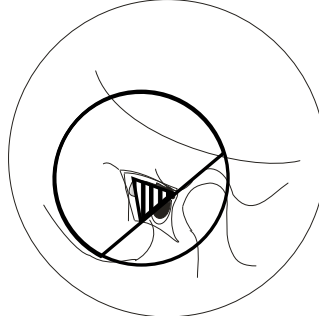
Unilateral Radiographic Conformations of the TB in Schuller’s Projection (URCOTEBS)	Event Index	White Balls (Weight of Healthy D-Cells) [%]	Black Balls (Weight of Diseased D-Cells) [%]	Corrected Primitive Probability (from the Unreturned Ball Scheme and Poisson’s Scheme) (Brought to 100%)	Mean Energy Consumption Relative to Consumption at the Time of Birth (q <sub>i</sub> )	Total Volume of Pneumatized Cavities Relative to the Volume at the time of Birth (v <sub>i</sub> )
1’	2’	3’	4’	5’	6	7’
a	0–5	95	5	$5.97 \times 10^{-1}$	10.72%	5.11
b	6–10	84	16	$7.54 \times 10^{-3}$	27.56%	3.14
c	11–13	76	24	$1.33 \times 10^{-1}$	39.80%	1.71
d	14–25	61	39	$2.62 \times 10^{-1}$	108.51%	1
Sum of calculated probabilities				1.00		

According to the law of large numbers (Moivre–Laplace), the frequency of general prevalence of the four unilateral radiographic conformations of the TB tends to be always the same for any given general human population (Table 5). Also see Table 6 for visual reference.

**Table 5.** The probabilities of Exclusive Random Events achievement constituted by the four Unilateral Radiographic Conformations (URCOTEBS): **URCOTEBS<sub>d</sub>**; **URCOTEBS<sub>c</sub>**; **URCOTEBS<sub>b</sub>**; **URCOTEBS<sub>a</sub>**.

Event Index	White Balls (Weight of Healthy D-Cells) [%]	Black Balls (Weight of Diseased D-Cells) [%]	Corrected Primitive Probability (from the Unreturned Ball Scheme and Poisson’s Scheme) (Brought to 100%)
2’	4’	5’	6’
0–5	95	5	$5.97 \times 10^{-1}$
6–10	84	16	$7.54 \times 10^{-3}$
11–13	76	24	$1.33 \times 10^{-1}$
14–25	61	39	$2.62 \times 10^{-1}$
Sum of calculated probabilities			1.00

**Table 6.** Schematic images of each URCOTEBS conformation.

	Health	Disease
a	 <p><b>A</b> P€ = 99.4%</p>	 <p><b>α</b> P€ = 0.6%</p>
b	 <p><b>B</b> P€ = 98.6%</p>	 <p><b>β</b> P€ = 1.4%</p>
c	 <p><b>C</b> P€ = 92.1%</p>	 <p><b>γ</b> P€ = 7.9%</p>
d	<p>Impossible event P€ = 0%</p>	
		 <p><b>δ</b> Certain event P€ = 100%</p>

### 3. Results

The aim of the study is to define an exact method for categorizing a unilateral radiographic scan of the TB (mastoid) in Schuller's projection (URCOTEBS) under one of the four conformations and using it for practical everyday clinical purposes.

The otic capsule (OC) achieves its maximum volume during the seventh month of fetal life and from the moment of birth has a maximum 2 mm. appositional growth only. In other words, if we consider the OC as a spherical object, the adult sphere is only 2 mm. larger than the newborn sphere. Based on these considerations, we can define the radiographic opacity of the OC as the gauge for measuring the projection area of the *Variable Geometry Peripheral Endo-temporal Bony Cavity Complex* or the *Anatomic Macroscopic Radiopaque Bony Support of the D-Organ*. For achieving graphic accuracy, we will circumscribe the radiographic opacity of the OC inside an equilateral triangle as a measuring reference. This is the most internal triangle of the orthogonal axial projection of the base of the regular composite geometric figure that is the geometric model of the TB in newborns and adults. This equilateral triangle has practically the same area in both newborns and adults. In Figure 7, we notice how the projection of the Non-variable Geometry Central Axial Bony Cavities of the Middle ear is inscribed within the triangle (Also see Figures 1 and 2).

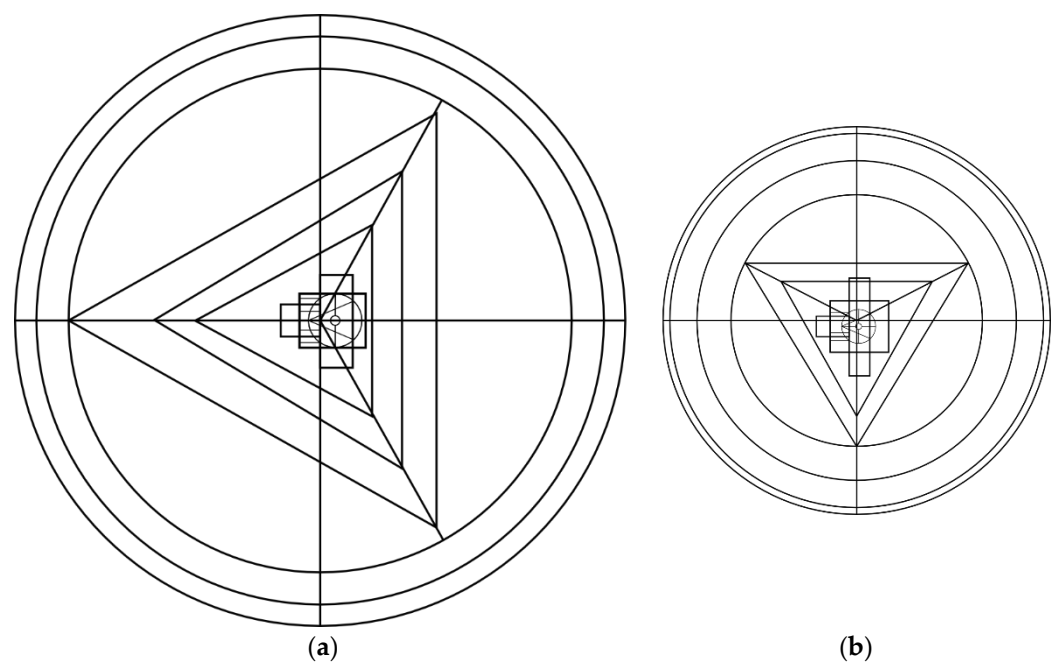


**Figure 7.** Axial orthogonal projections of the base of regular composed geometrical bodies representing the geometric-statistic model of the adult (a) and newborn (b) temporal bone. We can observe that the Central Axial Non-variable Geometry of the middle ears of adults and newborns has practically the same shape and size and that the equilateral triangles circumscribing it and the otic capsule are of the same areas.

The following graphic representations will depict the external circle of the orthogonal projection of the basis of the geometric figure in adults and the inner most equilateral triangle of the projection in newborns (Figure 7). We will also use a corresponding semicircle and the drawn schematics of a Schuller radiograph inscribed within the initial circle. By overlapping the three figures, namely the circle, semicircle, and drawing (Figure 8), we will establish the natural position of the initially described triangle. This triangle inscribes the projection of the following structures on radiographic film: OC opacity (bony labyrinth), non-variable geometry central axial middle ear (non-variable geometry cavities), coaxial transparency of the internal and external acoustic meatus. (Figures 7–12).

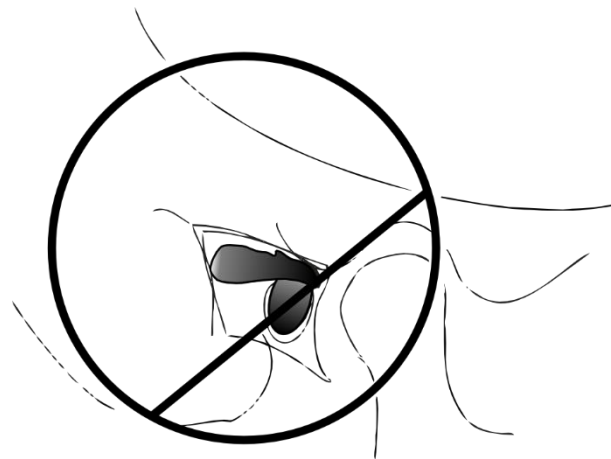
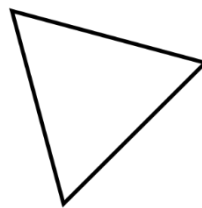


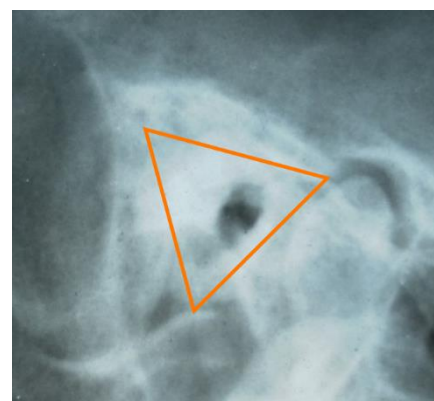
**Figure 8.** The schematic representation of an URCOTEBS radiograph with the circle and semicircle of the base of the orthogonal projection of the geometric body resulting from modelling the adult ME.



*URCOTEBS<sub>δ</sub>*



*Measuring gauge*



*Variable Geometry Peripheral Endo-temporal Bony Cavity Complex is stopped from development in the first 6–12 months after birth*

**Figure 9.** URCOTEBS<sub>δ</sub> is pathognomonic for the state of disease of the D-Organ, equivalent to the state of disease of the ME mucosa – Certain event P(E) = 100%.

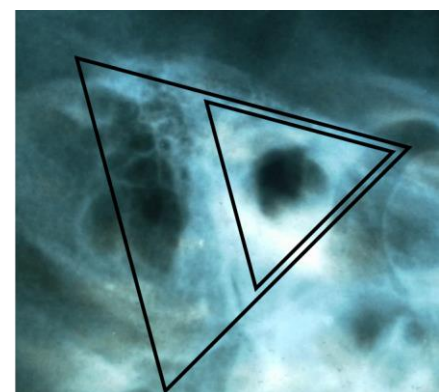
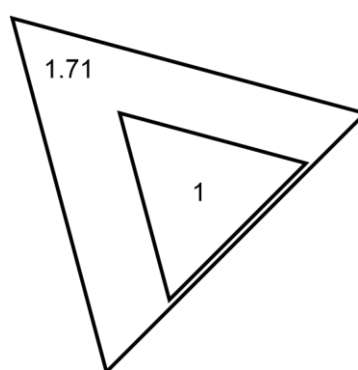


**Figure 10.** URCOTEBS<sub>c</sub>. The measuring gauge and the projection area of the Anatomic Macroscopic Radiopaque Peripheral Support of the D-Organ superimposed on the radiographic image of the TB. In the case of a URCOTEBS<sub>c</sub>, the projection area has a mean value 1.71 times larger than the gauge area (see Table 4, column 7).

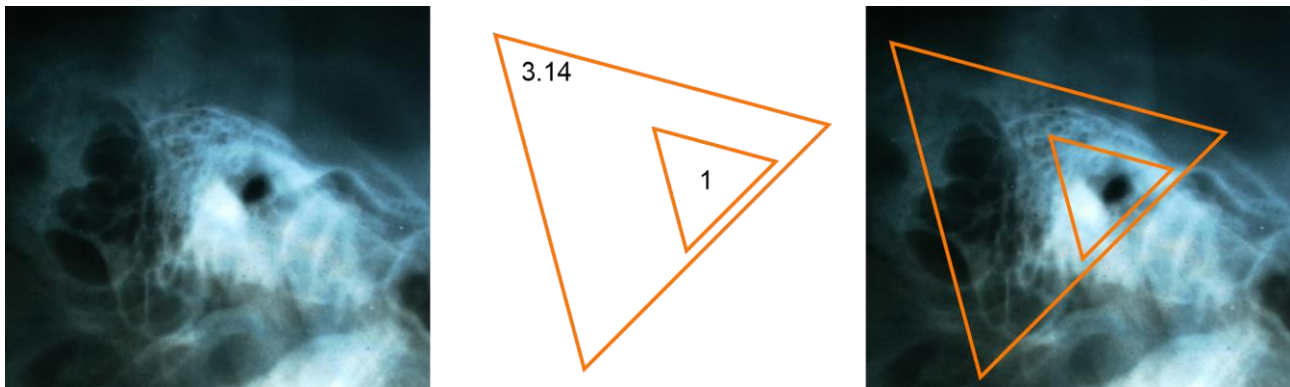


**Figure 11. URCOTEBS\_b.** The measuring gauge and the projection area of the Anatomic Macroscopic Radiopaque Peripheral Support of the D-Organ superimposed on the radiographic image of the TB. In the case of a **URCOTEBS\_b**, the projection area has a mean value 3.14 times larger than the gauge area (see Table 4, column 7).

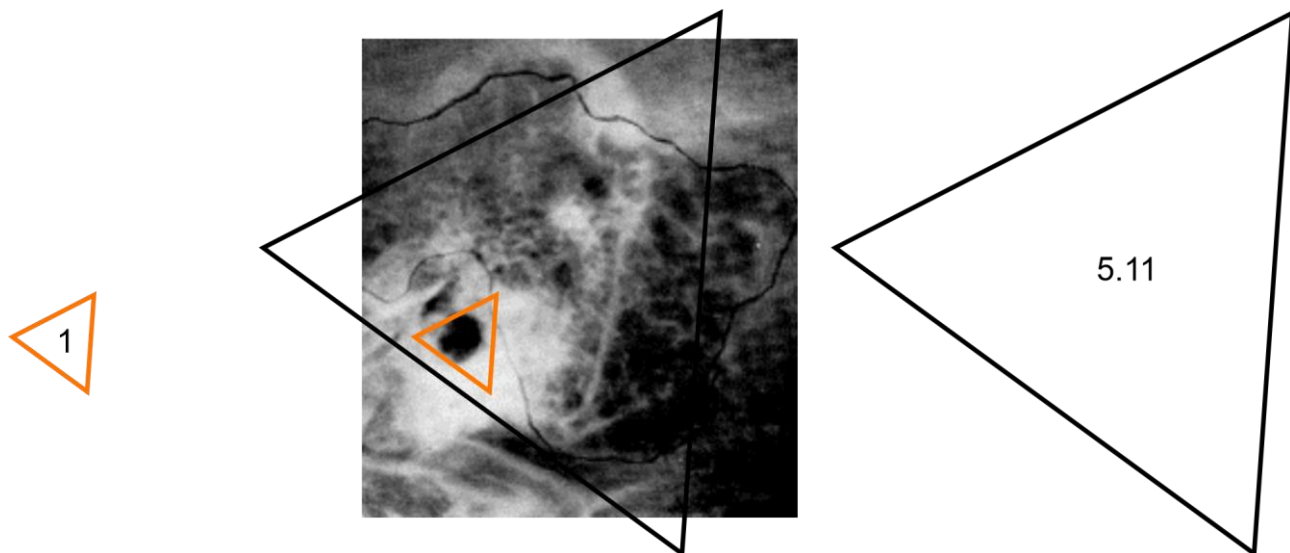


**Figure 12. URCOTEBS\_a.** The measuring gauge and the projection area of the Anatomic Macroscopic Radiopaque Peripheral Support of the D-Organ superimposed on the radiographic image of the TB. In the case of a **URCOTEBS\_a**, the projection area has a mean value 5.11 times larger than the gauge area (see Table 4, column 7).

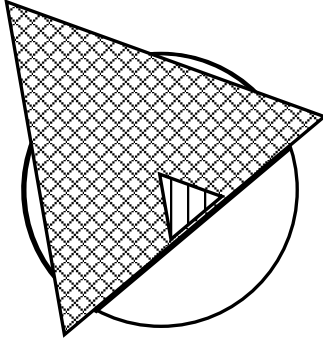
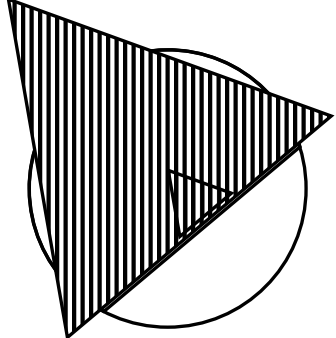
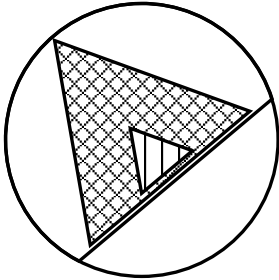
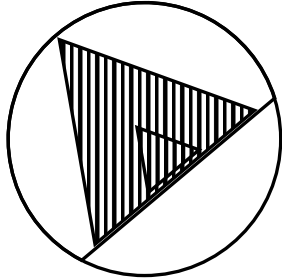
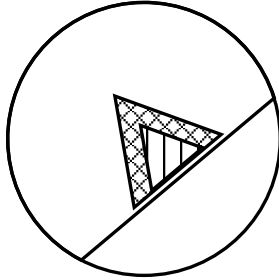
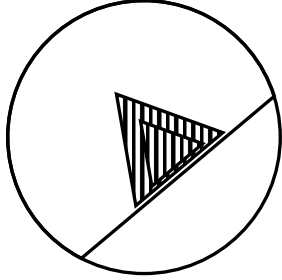
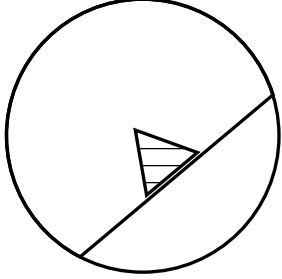
In this manner, we can describe schematic images of radiographs, analog icons, stylized icons, all of which represent the *unilateral radiographic conformations of the TB in Schuller's projection (URCOTEBS)*. See Tables 6–8.

From the previous paragraphs, we conclude that the equilateral triangle as a measuring gauge is implicitly present in any radiograph of any patient, and we only need to draw it upon the radiographic film (Figures 9–12). Thus, any radiograph of any patient will have its own measuring triangle and we will use a reference scale to measure the area of the *Anatomic Macroscopic Radiopaque Bony Support of the D-Organ*. This represents an enormous practical advantage. In other words, each image contains in itself the first division (0–1) and the first point (the equilateral triangle of point 1) of a unique measuring scale (reference scale). This means that the radiographic projection of the *Variable Geometry Peripheral Middle Ear* to be measured with this scale is outside the triangle gauge perimeter. We will draw next the contour of the *Variable Geometry Peripheral Middle Ear*, and this will be inscribed within an equilateral triangle larger than the gauge triangle as shown in Figures 9–12. Finally, we calculate the ratio between the area of the gauge and the

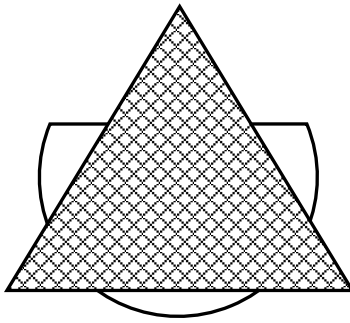
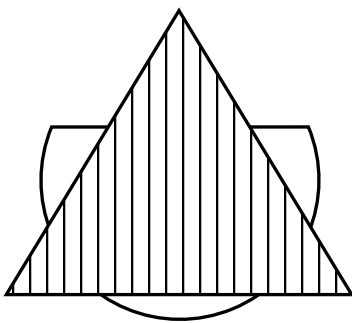
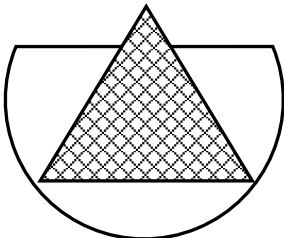
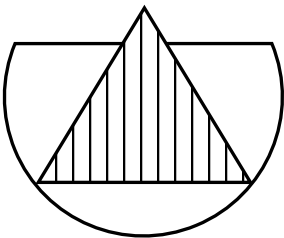
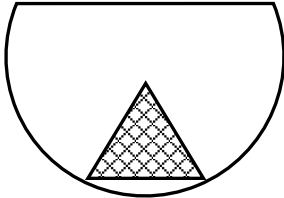
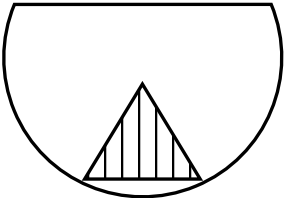
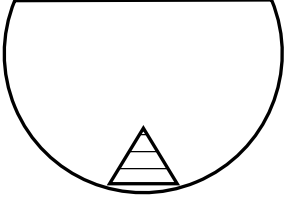


area of the projection triangle. Based on this numerical value and the values in the data matrix (Table 3, column 8 and Table 4, column 7), we can fit each unilateral radiographic image within one of the previously defined conformations (URCOTEBS\_d, URCOTEBS\_c, URCOTEBS\_b, URCOTEBS\_a).

**Table 7.** Analog icons for URCOTEBS.

	Health Icons	Disease Icons
<b>a</b>	 A	 $\alpha$
<b>b</b>	 B	 $\beta$
<b>c</b>	 C	 $\gamma$
<b>d</b>	Impossible Random Exclusive Event  non	 $\delta$

**Table 8.** Stylized icons for URCOTEBS.

	Health	Disease
a		
	A	$\alpha$
b		
	B	$\beta$
c		
	C	$\gamma$
d	Impossible Random Exclusive Event	
	Impossible event	$\delta$

In this manner, we can draw the following: schematic images of the radiographs of the four URCOTEBS (see Table 6), analog icons for URCOTEBS (Table 7), stylized icons for URCOTEBS (Table 8).

#### 4. Discussions

Starting from the conclusions that we already presented in our previous articles, we can safely state that the growth of the mastoid stops when the weight of diseased *D-Cells* is equal or higher than 28% [1,2]. Based on this, we can determine the growth rate of the *D-Organ* (Table 3, column 8 and Table 4, column 7). This growth is an analytical function of the weight of diseased *D-Cells*. Determining this ratio was achieved by defining the level of anatomic (geometric) development of the *D-Organ* at the moment of birth by the numerical value 1 and simply applying the rule of three.

Initially, only four numerical values for the weight of diseased *D-Cells* were determined  $\{[0; 0.27]; [0.28; 0.5]\}$  representing the limits of two variation intervals. These intervals have a very precise significance by defining the states of health and disease of the *D-Organ* [2]. The other previously undetermined values of the weight of diseased cells have been completely defined by approaching the pathology problem exclusively from a probability theory point of view.

We must now decode the statistic and probabilistic information encrypted in each type of **URCOTEBS** conformation. Each radiograph is encrypting statistic and stochastic data regarding the status of the *D-Organ*. We consider **URCOTEBS** a mirror that never lies about the *Danaid Organ*.

**URCOTEBS\_d** is, by definition, a radiographic image of the state of disease of the *D-Organ* [2]. Thus, the probability of disease in a **URCOTEBS\_d** is 100% [1]. This is a certain event probability [2], and this conformation is pathognomonic for *Chronic Inflammation of the ME Mucosa*. We must now determine the homologous probabilities for the other three conformations. The answer lies in the conclusion on the reasons for mastoid growth [2]. It is a question of metabolic energy economy for performing the *D-Function*. Once saved, it will be redistributed to defense mechanisms and other cellular function that require metabolic energy. This means that the probability of irreversible lesion is an analytical function of the energy consumption required for performing the *D-Function*. Thus, mastoid growth means increasing chances of maintaining health status [2].

A mathematical determination of the energy consumption reduction rate is identical to determining the volume growth rate. The data matrix (Table 3, column 6) contains numerical values for these determinations. Table 4 contains the processed values for the same determinations. Based on these values, we calculate the probability for disease presence for each of the three conformations—**URCOTEBS\_c**, **URCOTEBS\_b**, **URCOTEBS\_a**. The mathematical relations for these calculations (Equations (1)–(7)) are based on the rule of three. It is self-explanatory that, based on complementarity, we implicitly also determined the probability for health status (Tables 9 and 10, Equations (1)–(7)).

Middle-ear pathology leading to hearing loss is the most serious problem confronting the otologist, as the WHO estimates that between 65 and 330 million individuals suffer from some form of middle ear suppuration and that 50% of them suffer from hearing impairment, which could also be caused by a number of clinical and environmental factors [11–13]. The middle-ear or tympanic cavity is a very complicated structure, with notoriously intricate small-sized segments geometrically arranged as irregular interlinked spheroidal and polyhedral cavities. The geometry of the mastoid air cells system (MACS) has not been described for adults over a large range of MACS volumes [14], but numerous studies reports that these volumes are indirectly related to predisposition for middle-ear pathology such as chronic otitis media [15–19]. Measuring the size and pneumatization of the mastoid bone has been a current issue with otologists, as MACS functions as a gas reserve for the ME and slows the rate of middle-ear pressure decrease between Eustachian tube openings [20]. This would mean that MACS and not the Eustachian tube is the primary gas source for the ME [1,2,21]. The methods for measuring the volumes include the water-weight method, the pressurized transducer method, and planimetric methods [22–24].

The volume of interconnected air cells is difficult to measure, which is why various methods have been employed: researchers such as Palva et al., Csakanyi et al., and Valtonen et al., use planimetric methods [19,25–28], while others such as Koç et al., Vrabec et al., and Lee et al., advocate for volumetric methods [24–26,29–32]. An article by Park et al., reported that the MACS surface area is a linear function of the MACS volume [23]. This is also confirmed by the studies of Swarts et al., and Colhoun et al. [14,33], who used Schuller's projection X-rays and reconstructions from CT sections to document this linear relationship with a high correlation coefficient ( $r \approx 0.77$  and  $r \approx 0.95$ , respectively). The conclusion of

all this research is that relatively simple X-ray procedures can be used to screen ears for the MACS volume [14].

$$f(\alpha) = 1 - f(A) = \frac{1}{1 + \sum_{t=1}^5 \lambda \bar{q}_t(d; \Gamma_t) + \sum_{t=1}^5 \bar{q}(a) \bar{q}_t(d; \Gamma_t)} \tag{1}$$

$$f(\beta) = 1 - f(B) = \frac{1}{1 + \sum_{t=1}^5 \bar{q}(b) \bar{q}_t(d; \Gamma_t)} \tag{2}$$

$$f(\gamma) = 1 - f(C) = \frac{1}{1 + \sum_{t=1}^5 \bar{q}(c) \bar{q}_t(d; \Gamma_t)} \tag{3}$$

$$f(\delta) = 1; f(D) = 0 \tag{4}$$

Equations (1)–(4): Mathematical expressions of the probability of disease presence for each type of URCOTEBS [7–10].

$$\lambda = \frac{Q_{u_i}^{nb}}{Q_{u_i}^a} = \frac{\alpha A_a^D}{A_{nb}^D} = 7.87 \tag{5}$$

$$\theta = \frac{V_\varepsilon^a}{V_\varepsilon^{nb}} = 6.02 \tag{6}$$

$$V_\varepsilon = \frac{m_{\Omega_0}(q + 3)}{4W\bar{\rho}_\Omega} \tag{7}$$

Equations (5)–(7): The relations upon which the mathematical expressions of disease presence probability are founded for each type of URCOTEBS. These relations are the consequence of mathematical modeling (thermodynamic and geometric–statistical) of the structures and functions of the middle ear [1,2].

**Table 9.** Decoding stochastic information within any URCOTEBS, starting from the moment it was classified within one of the four conformations relative to the Disease Status of ME Mucosa.

Disease Status of D-Organ (Disease of the Middle-Ear Mucosa)								
URCOTEBS Generic Symbol	URCOTEBS Disease State Symbol	Initial Exclusive Random Event Index	Index Eveniment Aleator Exclusiv Ulterior	Initial White Balls (Mean Weight of Healthy D-Cells) [%]	Subsequent White Balls (Mean Weight of Healthy D-Cells) [%]	Initial Black Balls (Mean Weight of Diseased D-Cells) [%]	Subsequent Black Balls (Mean Weight of Diseased D-Cells) [%]	Probability
1	2	3	4	5	6	7	8	9
a	$\alpha$	0–5	14–25	95	61	5	39	0.60%
b	$\beta$	6–10	14–25	84	61	16	39	1.40%
c	$\gamma$	11–13	14–25	76	61	24	39	7.90%
d	$\delta$	14–25	no	61	no	39	no	100%

**Table 10.** Decoding stochastic information within any URCOTEBS, starting from the moment it was classified within one of the four conformations relative to the Health Status of ME Mucosa.

Health status of D-Organ (Health of the Middle-ear Mucosa)					
URCOTEBS Generic symbol	URCOTEBS Health State Symbol	Initial Exclusive Random Event Index	Initial White Balls (Mean Weight of Healthy D-Cells) [%]	Initial Black Balls (Mean Weight of Diseased D-Cells) [%]	Probability
1	2	3	4	5	6
a	A	0–5	95	5	99.40%
b	B	6–10	84	16	98.60%
c	C	11–13	76	24	92.10%

Due to the anatomic complexity, several mathematical models (static and dynamic behaviors) have been used to study ME function, all of them based on deterministic approaches [34–38]. Lumped element models, distributed parameter models, multi-body systems, and finite element models have been used to assess the function of the healthy ME [39,40], to evaluate pathological conditions [41], and also to verify results of ossicular chain reconstruction [42,43]. Because the high degree of variability among individuals leads to large discrepancies among samples, the ME behaves as an uncertain system, which means that stochastic models become very useful [34,44]. Modeling a dynamical system with uncertainties has been presented in the literature [45] and employs two groups of methods: parametric and nonparametric. Parametric approaches associate the uncertainties with the physical parameters of the system, and each parameter is treated as a random variable with a defined statistics, while nonparametric techniques deal with the uncertainties directly in the mathematical operators (matrices) of the system. The nonparametric probabilistic approach was proposed in 2000 by Soize et al., to consider the ME, and it was used to develop a stochastic model of the ME by Lobato et al., in 2022 [34,45,46]. It has also been applied in different contexts of uncertain structural dynamics, such as composite panels [34,47,48], automotive vehicles [34,49], drill-strings [34,50], and hermetic compressors [34,51]. Artificial intelligence (AI) shows promising results in the context of patient care, and several AI methods such as binary classification and logistic function could prove very useful for our future research [52]. Although the measuring gauge is currently manually drawn on the radiograph and is specific for each radiographic image, we envision the development of a software capable of directly applying the measuring gauge by using our theories. As previously shown, we use two equilateral triangles circumscribed to (1) the circular or oval transparency constituted by the almost total superimposing of the opacities of the two acoustic meati (external and internal); and (2) the opacity of the otic capsule and the tympanic bone. The second triangle circumscribes the endo-temporal cavity complex. We then calculate the ratio between the two surfaces to obtain the corresponding type of URCOTEBS.

Statistical calibration has also been used on geometry-based models such as the finite element (FE) model to calculate dynamic characteristics of the middle ear [39,53–56].

## 5. Conclusions

The unilateral radiographic image of the TB in Schuller's projection is a mirror that reflects the status of the ME mucosa, and URCOTEBS encodes the physiological state of the *D-Organ*. The present work gives the key to decoding this information into clinical language. The URCOTEBS matrix completely defines four types of unilateral radiographic conformations of the TB in Schuller's projection, which we termed, in ascending order of their projection areas (projection of their *Variable Geometry Peripheral Endo-temporal Bony Cavity Complex*) URCOTEBS\_d, URCOTEBS\_c, URCOTEBS\_b, and URCOTEBS\_a. The corresponding Greek letter designates the state of disease for each of these conformations: URCOTEBS\_δ, URCOTEBS\_γ, URCOTEBS\_β, URCOTEBS\_α, and the capital letters define their state of health: URCOTEBS\_D, URCOTEBS\_C, URCOTEBS\_B, URCOTEBS\_A.

URCOTEBS\_d is the smallest unilateral radiographic conformation of the TB in Schuller's projection and is, by definition, a radiographic image of the state of disease of the *D-Organ*. The probability of disease in a URCOTEBS\_d is 100%.

Starting from defining the *D-Organ*, we can now study all its essential aspects by using the unilateral radiographic image of the TB in Schuller's projection. This is achievable with stochastic analysis. These results are only a premise for future practical application. The discussion about the *D-Organ* as an *odd-numbered* organ is *necessary* but by no means *sufficient* both from a pathological and a clinical point of view, since both these perspectives require the study the *D-Organ* as a *pair*. This will be the subject of future work on **B**ilateral **R**adiographic **C**onformation of the **T**emporal **B**one in **S**chuller's projection (**BIRCOTEBS**). This radiographic system is very practical, cheap, readily available, and clinically usable as we defined in this paper.



A probabilistic reasoning is one that most people use to draw conclusions from incomplete or imperfect data. Even though measuring, reasoning, or communicating are possible without the use of probability theory, we consider it, as others have before us, indispensable and unavoidable in science. The material universe, including living creatures, is made up, as the name suggests, of matter. Some aspects of life will not be readily available for explanations employing current scientific techniques. It is not considered necessary nor possible to assume that living matter as analyzed by scientists could contain anything considered mysterious by a chemist or a physician. Thus, the fundamental laws of physical matter are nothing but the fundamental laws of any matter. Since the behavior of molecules, atoms, and elementary elements is analyzed with probabilistic theories by quantum physics, we must acknowledge the use of probabilistic estimations for the present topic as well.

Although famous scientists such as *Albert Einstein* (1879–1955) were unhappy with probabilistic foundations for science (“*God does not play dice*”), most members of the scientific community including such giants as *Niels Bohr* (1885–1962) or *Werner Heisenberg* (1901–1976) accept the modern rule or probability theory. If we understand that the most basic laws of elementary physical phenomena are probabilistic, we can acknowledge that probability theory is essential for many special scientific fields, including medicine.

**Author Contributions:** M.R., A.-C.N. and H.M. have contributed equally to this work and should, therefore, be considered first authors of this article. Conceptualization: M.R. and H.M.; methodology: M.R., H.M. and A.-C.N.; software: A.-I.M. and M.-A.S.; validation: M.R., A.-C.N. and H.M.; formal analysis: A.-I.M., H.M. and A.-C.N.; investigation: M.R., H.M. and A.-C.N.; resources: A.-I.M., M.-A.S. and H.M.; data curation: H.M., M.-A.S. and A.-I.M.; writing—original draft preparation: M.R. and H.M.; writing—review and editing: M.R. and A.-C.N.; visualization: M.R., H.M. and A.-C.N.; supervision: H.M. and M.R.; project administration: H.M., M.R. and A.-C.N. A.-I.M. and M.-A.S. have made substantial contributions to the acquisition, analysis, and interpretation of data and performed a final view of the article. A.-I.M. and M.-A.S. were also responsible of the data analysis and graphical representation of the results and performed a final view of the article. All authors have read and agreed to the published version of the manuscript.

**Funding:** This research received no external funding.

**Institutional Review Board Statement:** Not applicable.

**Informed Consent Statement:** Not applicable.

**Data Availability Statement:** Data are contained within the article.

**Conflicts of Interest:** The authors declare no conflict of interest.

## References

1. Rădulescu, M.; Mocanu, H.; Nechifor, A.; Mocanu, A.I. Thermodynamic Model for Middle-Ear Ventilation-Defining The D-Organ by Comparison to The Eustachian Tube (Re-Interpretation of A Classic Experiment and Review of Literature). *Acta Tech. Napocensis Ser. Appl. Mat. Mech. Eng.* **2022**, *65*, 69–78.
2. Rădulescu, M.; Mocanu, A.-I.; Dascălu, I.T.; Schipor, M.-A.; Mocanu, H. Geometric–Statistical Model for Middle-Ear Anatomy and Ventilation. *Appl. Sci.* **2022**, *12*, 11287. [CrossRef]
3. Broussais, F.J.V. *Traité de Physiologie Appliquée à la Pathologie*, 1822 ed.; Hachette BnF: Paris, France, 2013.
4. Canhuilhem, G. *On the Normal and the Pathological*; Reidel Publishing Company: Dordrecht, The Netherlands, 1978. [CrossRef]
5. Shelshakova, N.N. “Norm” and “Pathology”: A Comparative Analysis of Concepts. *Nat. Volatiles Essent. Oils* **2021**, *8*, 7377–7383.
6. Rostand, J. *Claude Bernard–Morceaux Choisis, Cap I, Leçons de Physiologie Experimentale appliquée à la Médecine, Sur le Rôle de L’anatomie Dans la Découverte des Fonctions*, Septième ed.; Gallimard: Paris, France, 1938; pp. 37–48. (In French)
7. Văduva, I. On a Particular Lifetime Distribution. *Rev. Air Force Acad.* **2017**, *2*, 5–14. [CrossRef]
8. Fricker, C.; Guillemin, F.; Robert, P. An Identification Problem in an Urn and Ball Model with Heavy Tailed Distributions. *Probab. Eng. Informational Sci.* **2010**, *24*, 77–97. [CrossRef]
9. Busbee, B. Uses of the Hypergeometric Distribution for Determining Survival or Complete Representation of Subpopulations in Sequential Sampling. Master’s Thesis. Electronic Theses and Dissertations, Stephen F Austin State University, Nacogdoches, TX, USA, 2017; p. 118. Available online: <https://scholarworks.sfasu.edu/etds/118> (accessed on 23 November 2023).
10. Ghitany, M.E.; Al-Mutairi, D.K.; Nadarajah, S. Zero-truncated Poisson–Lindley distribution and its application. *Math. Comput. Simul.* **2008**, *79*, 279–287. [CrossRef]

11. Neagu, A.C.; Budişteanu, M.; Gheorghe, D.C.; Mocanu, A.I.; Mocanu, H. Rare Gene Mutations in Romanian Hypoacusis Patients: Case Series and a Review of the Literature. *Medicina* **2022**, *58*, 1252. [[CrossRef](#)] [[PubMed](#)]
12. Mocanu, H. The role of perinatal hearing screening in the normal development of the infant's language. In *Debating Globalization. Identity, Nation and Dialogue*, 4th ed.; Boldea, I., Sigmirean, C., Eds.; Arhipeleag XXI Press: Tirgu Mures, Romania, 2017; pp. 562–569.
13. Mocanu, H. The economic impact of early diagnosis of congenital hearing loss. In *Debating Globalization. Identity, Nation and Dialogue*, 4th ed.; Boldea, I., Sigmirean, C., Eds.; Arhipeleag XXI Press: Tirgu Mures, Romania, 2017; pp. 556–561.
14. Swarts, J.D.; Doyle, B.M.C.; Doyle, W.J. Surface Area-Volume Relationships for the Mastoid Air Cell System in Adult Humans. *J. Laryngol. Otol.* **2011**, *125*, 580–584. [[CrossRef](#)]
15. Sade, J.; Fuchs, C. A comparison of mastoid pneumatization in adults and children with cholesteatoma. *Eur. Arch. Otorhinolaryngol.* **1994**, *251*, 191–195. [[CrossRef](#)]
16. Sade, J.; Fuchs, C. Secretory Otitis Media in Adults: I. The Role of Mastoid Pneumatization as a Risk Factor. *Ann. Otol. Rhinol. Laryngol.* **1996**, *105*, 643–647. [[CrossRef](#)]
17. Sadé, J.; Fuchs, C. Secretory Otitis Media in Adults: II. The Role of Mastoid Pneumatization as a Prognostic Factor. *Ann. Otol. Rhinol. Laryngol.* **1997**, *106*, 37–40. [[CrossRef](#)]
18. Lesinskas, E. Factors affecting the results of nonsurgical treatment of secretory otitis media in adults. *Auris Nasus Larynx* **2003**, *30*, 7–14. [[CrossRef](#)] [[PubMed](#)]
19. Valtonen, H.J.; Dietz, A.; Qvarnberg, Y.H.; Nuutinen, J. Development of Mastoid Air Cell System in Children Treated with Ventilation Tubes for Early-Onset Otitis Media: A Prospective Radiographic 5-Year Follow-Up Study. *Laryngoscope* **2005**, *115*, 268–273. [[CrossRef](#)] [[PubMed](#)]
20. Doyle, W.J. The mastoid as a functional rate-limiter of middle ear pressure change. *Int. J. Pediatr. Otorhinolaryngol.* **2007**, *71*, 393–402. [[CrossRef](#)] [[PubMed](#)]
21. Cohen, D.; Raveh, D.; Peleg, U.; Nazarian, Y.; Perez, R. Ventilation and clearance of the middle ear. *J. Laryngol. Otol.* **2009**, *123*, 1314–1320. [[CrossRef](#)] [[PubMed](#)]
22. Byun, S.W.; Lee, S.-S.; Park, J.Y.; Yoo, J.H. Normal Mastoid Air Cell System Geometry: Has Surface Area Been Overestimated? *Clin. Exp. Otorhinolaryngol.* **2016**, *9*, 27–32. [[CrossRef](#)] [[PubMed](#)]
23. Park, M.S.; Yoo, S.H.; Lee, D.H. Measurement of surface area in human mastoid air cell system. *J. Laryngol. Otol.* **2000**, *114*, 93–96. [[CrossRef](#)]
24. Koç, A.; Ekinçi, G.; Bilgili, A.M.; Akpınar, I.N.; Yakut, H.; Han, T. Evaluation of the mastoid air cell system by high resolution computed tomography: Three-dimensional multiplanar volume rendering technique. *J. Laryngol. Otol.* **2003**, *117*, 595–598. [[CrossRef](#)]
25. Palva, T.; Palva, A. Size of the Human Mastoid System. *Acta. Otolaryngol. Stockh.* **1966**, *62*, 237–251. [[CrossRef](#)]
26. Csakanyi, Z.; Katona, G.; Josvai, E.; Mohos, F.; Sziklai, I. Volume and Surface of the Mastoid Cell System in Otitis Media with Effusion in Children: A Case-Control Study by Three-Dimensional Reconstruction of Computed Tomographic Images. *Otol. Neurotol.* **2011**, *32*, 64–70. [[CrossRef](#)]
27. Cinamon, U. The growth rate and size of the mastoid air cell system and mastoid bone: A review and reference. *Eur. Arch. Oto-Rhino-Laryngol.* **2009**, *266*, 781–786. [[CrossRef](#)]
28. Hug, J.E.; Pfaltz, C.R. Temporal bone pneumatization. A planimetric study. *Arch. Otorhinolaryngol.* **1981**, *233*, 145–156. [[CrossRef](#)]
29. Flisberg, K.; Zsigmond, M. The Size of the Mastoid Air Cell System: *Planimetry—Direct Volume Determination*. *Acta Oto-Laryngol.* **1965**, *60*, 23–29. [[CrossRef](#)]
30. Todd, N.W.; Pitts, R.B.; Braun, I.F.; Heindel, H. Mastoid size determined with lateral radiographs and computerized tomography. *Acta Otolaryngol.* **1987**, *103*, 226–231. [[CrossRef](#)] [[PubMed](#)]
31. Vrabec, J.T.; Champion, S.W.; Gomez, J.D.; Johnson, R.F., Jr.; Chaljub, G. 3D CT imaging method for measuring temporal bone aeration. *Acta. Otolaryngol.* **2002**, *122*, 831–835. [[CrossRef](#)] [[PubMed](#)]
32. Lee, D.H.; Jun, B.C.; Kim, D.G.; Jung, M.K.; Yeo, S.W. Volume variation of mastoid pneumatization in different age groups: A study by three-dimensional reconstruction based on computed tomography images. *Surg. Radiol. Anat.* **2005**, *27*, 37–42. [[CrossRef](#)]
33. Colhoun, E.N.; O'Neill, G.; Francis, K.R.; Hayward, C. A comparison between area and volume measurements of the mastoid air spaces in normal temporal bones. *Clin. Otolaryngol. Allied Sci.* **1988**, *13*, 59–63. [[CrossRef](#)] [[PubMed](#)]
34. Lobato, L.C.; Paul, S.; Cordioli, J.A.; Ritto, T.G. Stochastic model of the human middle ear using a nonparametric probabilistic approach. *J. Acoust. Soc. Am.* **2022**, *151*, 2055–2065. [[CrossRef](#)]
35. De Greef, D.; Buytaert, J.A.; Aerts, J.R.; Van Hoorebeke, L.; Dierick, M.; Dirckx, J. Details of human middle ear morphology based on micro-CT imaging of phosphotungstic acid stained samples. *J. Morphol.* **2015**, *276*, 1025–1046. [[CrossRef](#)]
36. Rosowski, J.; Chien, W.; Ravicz, M.; Merchant, S. Testing a Method for Quantifying the Output of Implantable Middle Ear Hearing Devices. *Audiol. Neurotol.* **2007**, *12*, 265–276. [[CrossRef](#)]
37. Funnell, W.R.J.; Maftoon, N.; Decraemer, W.F. *Modeling of Middle Ear Mechanics*; Springer: New York, NY, USA, 2013; pp. 171–210.
38. Paolis, A.D.; Bikson, M.; Nelson, J.T.; de Ru, J.A.; Packer, M.; Cardoso, L. Analytical and numerical modeling of the hearing system: Advances towards the assessment of hearing damage. *Hear. Res.* **2017**, *349*, 111–128. [[CrossRef](#)]

39. Koike, T.; Wada, H.; Kobayashi, T. Modeling of the human middle ear using the finite-element method. *J. Acoust. Soc. Am.* **2002**, *111*, 1306–1317. [[CrossRef](#)]
40. Lobato, L.; Paul, S.; Cordioli, J. Statistical analysis of the human middle ear mechanical properties. *J. Acoust. Soc. Am.* **2022**, *151*, 2043–2054. [[CrossRef](#)]
41. Gan, R.Z.; Cheng, T.; Dai, C.; Yang, F.; Wood, M.W. Finite element modeling of sound transmission with perforations of tympanic membrane. *J. Acoust. Soc. Am.* **2009**, *126*, 243–253. [[CrossRef](#)] [[PubMed](#)]
42. Neudert, M.; Bornitz, M.; Mocanu, H.; Lasurashvili, N.; Beleites, T.; Offergeld, C.; Zahnert, T. Feasibility Study of a Mechanical Real-Time Feedback System for Optimizing the Sound Transfer in the Reconstructed Middle Ear. *Otol. Neurotol* **2018**, *39*, e907–e920. [[CrossRef](#)] [[PubMed](#)]
43. Mocanu, H.; Bornitz, M.; Lasurashvili, N.; Zahnert, T. Evaluation of Vibrant® Soundbridge™ positioning and results with laser doppler vibrometry and the finite element model. *Exp. Ther. Med.* **2021**, *21*, 262. [[CrossRef](#)] [[PubMed](#)]
44. Ebrahimi, A.; Maftoon, N. Stochastic finite element modelling of human middle-ear. In Proceedings of the 44th Conference of The Canadian Medical and Biological Engineering, Virtual Conference, 11–13 May 2021; Volume 44.
45. Daouk, S.; Louf, F.; Dorival, O.; Champaney, L.; Audebert, S. Uncertainties in structural dynamics: Overview and comparative analysis of methods. *Mech. Ind.* **2015**, *16*, 404. [[CrossRef](#)]
46. Soize, C. A nonparametric model of random uncertainties for reduced matrix models in structural dynamics. *Probabilistic Eng. Mech.* **2000**, *15*, 277–294. [[CrossRef](#)]
47. Chen, C.; Duhamel, D.; Soize, C. Probabilistic approach for model and data uncertainties and its experimental identification in structural dynamics: Case of composite sandwich panels. *J. Sound Vib.* **2006**, *294*, 64–81. [[CrossRef](#)]
48. Petrescu, S.M.S.; Țuculina, M.J.; Popa, D.L.; Duță, A.; Salan, A.I.; Voinea Georgescu, R.; Diaconu, O.A.; Turcu, A.A.; Mocanu, H.; Nicola, A.G.; et al. Modeling and Simulating an Orthodontic System Using Virtual Methods. *Diagnostics* **2022**, *12*, 1296. [[CrossRef](#)] [[PubMed](#)]
49. Durand, J.-F.; Soize, C.; Gagliardini, L. Structural-acoustic modeling of automotive vehicles in presence of uncertainties and experimental identification and validation. *J. Acoust. Soc. Am.* **2008**, *124*, 1513–1525. [[CrossRef](#)] [[PubMed](#)]
50. Ritto, T.; Soize, C.; Sampaio, R. Robust optimization of the rate of penetration of a drill-string using a stochastic nonlinear dynamical model. *Comput. Mech.* **2010**, *45*, 415–427. [[CrossRef](#)]
51. Fontanela, F.; Silva, O.; Lenzi, A.; Ritto, T. Development of a stochastic dynamical model for hermetic compressor components with experimental investigation. *Mech. Syst. Sign. Process.* **2016**, *76*, 712–728. [[CrossRef](#)]
52. Kufel, J.; Bargiel-Łączek, K.; Kocot, S.; Koźlik, M.; Bartnikowska, W.; Janik, M.; Czogalik, Ł.; Dudek, P.; Magiera, M.; Lis, A.; et al. What Is Machine Learning, Artificial Neural Networks and Deep Learning? —Examples of Practical Applications in Medicine. *Diagnostics* **2023**, *13*, 2582. [[CrossRef](#)] [[PubMed](#)]
53. Lee, D.; Ahn, T.-S. Statistical calibration of a finite element model for human middle ear. *J. Mech. Sci. Technol.* **2015**, *29*, 2803–2815. [[CrossRef](#)]
54. Vollandri, G.; Di Puccio, F.; Forte, P.; Manetti, S. Model-oriented review and multi-body simulation of the ossicular chain of the human middle ear. *Med. Eng. Phys.* **2012**, *34*, 1339–1355. [[CrossRef](#)]
55. Gan, R.; Reeves, B.; Wang, X. Modeling of sound transmission from ear canal to cochlea. *Ann. Biomed. Eng.* **2007**, *35*, 2180–2195. [[CrossRef](#)]
56. Gan, R.Z.; Sun, Q.; Feng, B.; Wood, M.W. Acoustic structural coupled finite element analysis for sound transmission in human ear—Pressure distributions. *Med. Eng. Phys.* **2006**, *28*, 395–404. [[CrossRef](#)]

**Disclaimer/Publisher’s Note:** The statements, opinions and data contained in all publications are solely those of the individual author(s) and contributor(s) and not of MDPI and/or the editor(s). MDPI and/or the editor(s) disclaim responsibility for any injury to people or property resulting from any ideas, methods, instructions or products referred to in the content.